Corrosion Science 120 (2017) 1–13

Contents lists available at ScienceDirect

Corrosion Science

journal homepage: www.elsevier.com/locate/corsci

Atomic diffusion induced degradation in bimetallic layer coated cemented tungsten carbide

Zirong Peng [a], Michael Rohwerder [a,*], Pyuck-Pa Choi [a,b], Baptiste Gault [a,*], Thorsten Meiners [a], Marcel Friedrichs [c], Holger Kreilkamp [c], Fritz Klocke [c], Dierk Raabe [a]

[a] Max-Planck Institut für Eisenforschung GmbH, Max-Planck Str. 1, 40237 Düsseldorf, Germany
[b] Korea Advanced Institute of Science and Technology (KAIST), Department of Materials Science and Engineering, Daejeon 305-338, Republic of Korea
[c] Fraunhofer Institute for Production Technology (IPT), Steinbachstrasse 17, 52074 Aachen, Germany

ARTICLE INFO

Article history:
Received 2 December 2016
Received in revised form 12 January 2017
Accepted 13 January 2017
Available online 20 February 2017

Keywords:
A. Metal coatings
A. Sputtered film
B. TEM
C. Oxidation
C. Interfaces

ABSTRACT

We investigated the temporal degradation of glass moulding dies, made of cemented tungsten carbide coated with PtIr on an adhesive Cr or Ni interlayer, by electron microscopy and atom probe tomography. During the exposure treatments at 630 °C under an oxygen partial pressure of 1.12×10^{-23} bar, Cr (Ni) was found to diffuse outwards via grain boundaries in the PtIr, altering the surface morphology. Upon dissolution of the interlayer, the WC substrate also started degrading. Extensive interdiffusion processes involving PtIr, Cr (Ni) and WC took place, leading to the formation of intermetallic phases and voids, deteriorating the adhesion of the coating.

1. Introduction

Multilayer coatings or thin films have various application fields. They are frequently utilised in engineering components, tools and moulds as well as microelectronic, magnetic and optical devices [1–4]. Compared to single layer coatings, multilayer coatings, combining beneficial properties of different materials, may fulfil several practical requirements at once. They may also be useful in cases where only applying a single layer coating may not be sufficient. An important example is the use of an interfacial bonding layer between the top coating and the substrate to enhance adhesion [5–8]. However, multi-layered structures are commonly thermodynamically unstable. There is a strong driving force for interdiffusion and reaction, which will be detrimental to thermal stability of the coating unless kinetics of these processes are slow. Unfortunately, the typical fine-grained microstructure of thin films as well as large surface and interface areas provide numerous high diffusivity paths. Together with the short diffusion distances naturally associated with thin coatings, tremendous compositional changes can arise and new phases as well as voids can form, which will considerably deteriorate the coating properties [9–12].

Here, we report on the temporal degradation of a bimetallic layer coating deposited on cemented tungsten carbide substrate during isothermal exposures under an oxygen partial pressure of 1.12×10^{-23} bar at 630 °C. The coating consists of an ~650-nm-thick PtIr top layer and an ~20-nm-thick intermediate layer of metallic Cr or Ni (PtIr/Cr or PtIr/Ni), which is frequently utilised in moulds for precision glass moulding (PGM) [13–15]. It is a promising and worldwide employed process for manufacturing high quality optical products with complex-geometries. During PGM, glass blanks are placed in the mould of a pressing tool and are heated under vacuum or N_2 protective atmosphere up to the glass forming temperature, which normally ranges from 400 to 700 °C. Subsequently, high press forces (2–20 kN) are applied for several minutes until the mould form is homogeneously filled with glass. After controlled cooling, the final products can be detached from the mould [16–18]. PtIr, as a noble metal based coating, is chemically inactive and does not stick to glass. An intermediate layer, Cr or Ni, is used to improve the adhesion strength between base material and top coating [19,20]. Due to the harsh operating condition during glass pressing where intense thermal, chemical and mechanical forces are imposed simultaneously, coating degradation takes place very fast and becomes a severe problem, strongly limiting the service lifetime of moulds [21–23]. Since the produc-

* Corresponding authors.
E-mail addresses: rohwerder@mpie.de (M. Rohwerder), b.gault@mpie.de (B. Gault).

http://dx.doi.org/10.1016/j.corsci.2017.01.007

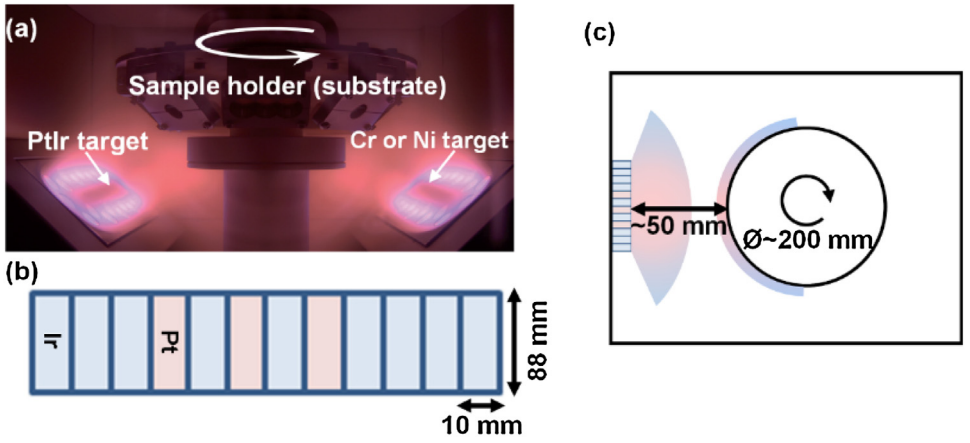

Fig. 1. (a) Configuration of the deposition chamber. (b) Sketch showing the arrangement of the pure Ir and Pt pieces within the target. (c) Schematic drawing of the top view of the deposition chamber to illustrate the coating process of the PtIr layer.

tion costs are directly related to the mould lifetime, designing high-performance and high-durability moulds as well as developing concepts to impede their degradation have become a top priority for the PGM industry. A key to achieve this goal is the understanding of the fundamental degradation mechanisms of mould materials such as PtIr/Cr/WC and PtIr/Ni/WC.

In previous studies, the reliability and stability of diverse metallic multilayer thin films have been investigated, e.g. Cu/Sn [24], Au/Ni/Cr [25], Cu/Ta [26], Pt/Ti-W [27], MoRu/Cr/Ti [28], PtIr/Ni [23,29], and PtIr/Cr [15,23], by means of a variety of analytical techniques such as X-ray diffraction (XRD), Rutherford backscattering spectroscopy (RBS), Auger electron spectroscopy (AES), energy-dispersive X-ray spectroscopy (EDS), X-ray photoelectron spectroscopy (XPS) and secondary ion mass spectroscopy (SIMS) [29–32]. However, the spatial resolution and detection sensitivity of these techniques was not sufficient to reveal the diffusion and segregation phenomena at grain boundaries, and limited insights were gained on the degradation mechanisms. Atom probe tomography (APT) is a unique technique, which has the capability to reveal three-dimensional (3D) chemical information at (sub-)nanometre scale with high sensitivity (in the range of tens of part-per-million) and which has been successfully applied to thin film materials [33–38]. Therefore, in this work we applied APT to study diffusion and degradation phenomena in PtIr/Cr/WC and PtIr/Ni/WC. In addition to APT, we also use scanning electron microscopy (SEM) and (scanning) transmission electron microscopy ((S)TEM) for microstructural analysis and STEM-EDS and AES for chemical analysis.

2. Material and methods

2.1. Specimen preparation

The base material was nano-grain sized cemented tungsten carbide containing around 0.3 wt.% Co binder (CTN01L, Ceratizit S.A). Before coating, bulk substrate samples were grinded and polished, making their surface roughness Ra smaller than 5 nm. Subsequently, the samples were cleaned in an ultrasonic bath (SurTec 089/131, SurTec International GmbH). The coating process was accomplished in a magnetron sputtering unit (CemeCon CC800/9). The configuration of the deposition chamber is shown in Fig. 1(a). Before coating, a plasma etching process was carried out to clean and activate the substrate surface to ensure a good adhesion. Subsequently, a Cr or Ni layer of about 20 nm in thickness and an ~650-nm-thick PtIr top coating were deposited sequentially. The detailed parameters of the coating process are listed in Table 1. The PtIr target used in this study is home-made, and is not a PtIr alloy but consists of three pieces of pure Pt stacked with nine pieces of pure Ir, as shown in Fig. 1(b).

2.2. Exposure treatment

A novel laboratory set-up was used to induce degradation of the coating, with which the exposure conditions e.g. time, atmosphere and temperature can be accurately controlled [39]. Mimicking the real PGM process, the treatment temperature was set to be 630 °C and the furnace atmosphere was selected as 97.5%N_2-2.5%H_2 with the dew point (DP) of +20 °C. The DP is manipulated by forcing the gas mixture through columns which are filled with water. By adjusting their temperature, desired dew points can be obtained. Under these conditions, the resulting oxygen partial pressure was calculated to be approximately 1.12×10^{-23} bar. Such a low oxygen partial pressure is desirable for controlling coating degradation. Thereby, the successive stages of the degradation process can be accessed simply by adjusting the exposure time. Moreover, the partial pressure of oxygen is kept high enough to oxidise Cr but not Ni, so the effects of oxidation on degradation can be separated and studied individually. During the real PGM processes, the oxygen partial pressures in the PGM machine were estimated to lie in the range of 10^{-6} bar, much higher than the partial pressure we applied in this study. In real processing systems, it is determined by the leakage rate of the system and thermodynamically not well defined. The H_2O/H_2 equilibrium conditions used in this study provide full thermodynamic control. In this work, results will be shown for the PtIr/Cr/WC system in the as-fabricated state, as well as after 6 h, 18 h, and 168 h exposure at 630 °C under the above-described condition ($P_{O2} \approx 1.12 \times 10^{-23}$ bar) in order to illustrate the evolution of degradation. As for the PtIr/Ni/WC system, only representative results for the 48h-exposed specimen will be shown, since the observed degradation mechanism is very similar to that in the PtIr/Cr/WC system. It is worth to mention that although in order to be able to resolve the successive stages of the degradation, especially the early stages, the partial pressure of oxygen in the atmosphere used here is much lower than that in the actual processing, we do not expect an effect on the degradation mechanisms. We also analysed samples obtained from a technical set-up and found the same degradation features. Furthermore, the fact that the degradation mechanisms observed in the PtIr/Cr/WC and PtIr/Ni/WC systems are very similar is also a proof that the degradation mechanism is not strongly affected by the oxygen activity.

Table 1
Detailed parameters for layer deposition process.

Target	Etching –	Interlayer deposition Chromium or nickel (99.9%)	PtIr layer deposition Platinum (99.99%) and iridium (99.9%)
Heating power/kW	0	2	2
Argon pressure/mPa	390	200	200
Bias voltage/V (f = 240 kHz)	650	60	60
Cathode power/W (f = 50 kHz)	–	125	250
Table revolution/rpm	2.5	2.5	2.5
Time/min	15	4	40
Thickness/nm	–	~20	~650

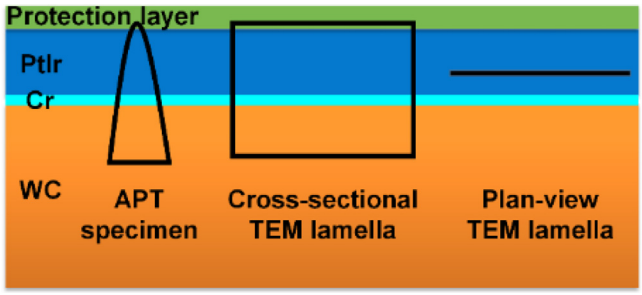

Fig. 2. Sketch to illustrate the position and orientation of APT and (S)TEM specimens.

2.3. Specimen characterisation

Both APT and (S)TEM specimens were fabricated using a dual beam focused-ion-beam (FIB) instrument (FEI Helios Nanolab 600/600i) and the in-situ lift-out method [40,41]. As illustrated in Fig. 2, the APT specimens were prepared with an alignment perpendicular to the sample surface, so that the analysis direction is parallel to the coating growth direction. For the (S)TEM measurements, both cross-sectional (perpendicular to the sample surface) and plan-view (parallel to the sample surface) lamellae were prepared. To remove regions severely damaged by the high-energy (30 kV) Ga ion beam during APT specimens and (S)TEM lamellae fabrication, a final cleaning procedure was carried out at 2 kV and 28 pA. APT measurements were conducted using a LEAP^{TM} 3000X HR (Cameca Instruments) instrument, equipped with a reflectron lens. Laser pulsing mode (532 nm wavelength, ~10 μm spot size) was applied at a pulse repetition rate of 250 kHz and a pulse energy of 0.8 nJ. The specimen base temperature was kept at 60 K and the target detection rate was set to be 0.2% (2 ions detected every 1000 pulses). These analysis parameters were optimised according to a previous work [42]. (S)TEM images were acquired using a JEOL JEM-2200FS microscope with 200 kV accelerating voltage (Figs. 3 (b), 5(b), 6(a), 10(a), 11(b), 12(a), 13(a), 15(a), 17) STEM-EDS were performed using a probe-corrected FEI Titan Themis 60–300 S/TEM with 300 kV accelerating voltage using a Super-X windowless EDS detector. Correspondingly a high-angle annular dark field (HAADF) image was taken from the measured region using a Fischione HAADF detector (Fischione Instruments) (Fig. 8). AES measurements were conducted with a JEOL JAMP-9500F system equipped with a hemispherical analyser. The field emission electron gun operated at an acceleration voltage of 25 keV and a

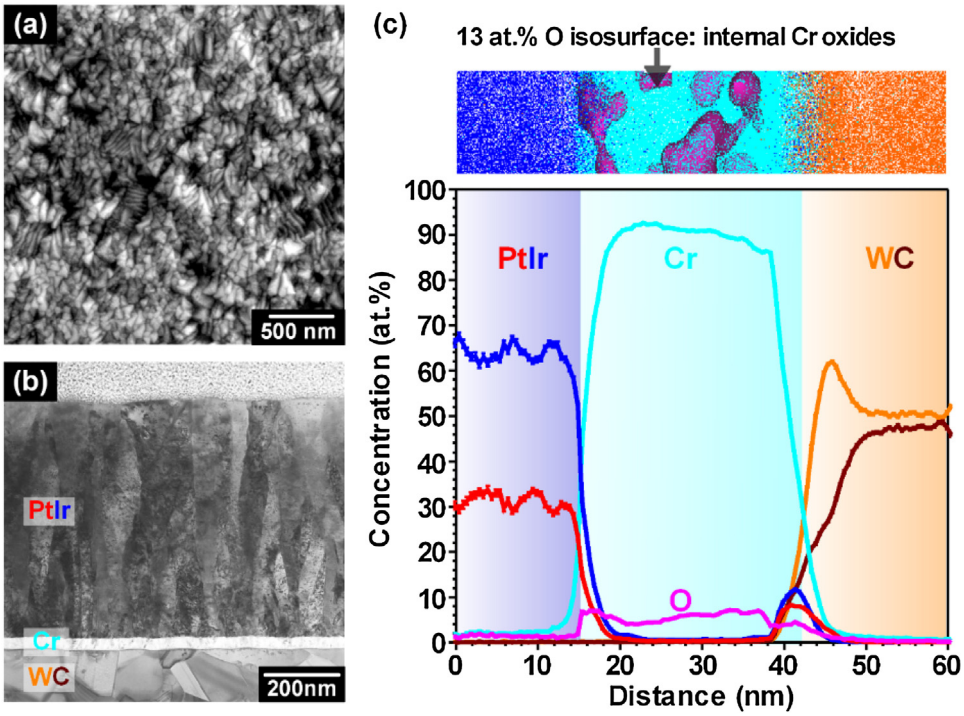

Fig. 3. Representative characterisation results obtained from the as-fabricated PtIr/Cr/WC specimen: (a) Surface SEM image, (b) cross-sectional BF STEM image, and (c) 1D concentration profile and a corresponding clipped atom map across the Cr layer. For clarity, only Ir (blue), Cr (cyan), O (magenta) and W ions (orange) are shown. The 13 at.% O iso-concentration surfaces represent the small Cr oxides found inside the Cr layer. (For interpretation of the references to colour in this figure legend, the reader is referred to the web version of this article.)

beam current of 10 nA. AES peaks of Pt MNN, Ir MNN and Cr LMM were recorded and used.

3. Results

3.1. PtIr/Cr/WC specimen

3.1.1. As-fabricated state

The surface SEM and cross-sectional bright-field (BF) STEM micrographs of the as-fabricated PtIr/Cr/WC sample are shown in Fig. 3(a) and (b), respectively. The PtIr and Cr layers as well as the WC substrate can be clearly identified in the STEM image. They exhibit distinctly different microstructures. As commonly observed for sputtered films, the PtIr layer consists of very fine columnar grains, growing along the deposition direction. Individual grains can be distinguished by differences in contrast, where the grain sizes range from 50 to 100 nm. The thickness of the Cr layer is uniform. Both PtIr/Cr and Cr/WC interfaces appear flat and sharp. No voids or cracks can be observed. APT analyses of the PtIr layer show that the overall atomic ratio between Ir and Pt is around 2, matching the target value. However, periodic Ir- and Pt-rich sublayers were observed (see Figs. 3(c) and 14(b)), which can be attributed to the combination of the PtIr target and substrate rotation during the deposition. As illustrated in Fig. 1, the non-uniform arrangement of the Pt and Ir pieces in the PtIr target can lead to an inhomogeneous distribution of Pt and Ir ions in the plasma flux. When the substrate is directly facing the target, the content of Pt will be slightly higher, while, when it moves away, Ir content will increase. With the rotation of the substrate, this concentration variation will appear periodically. Similar phenomena have been reported in several previous studies [43–45]. The atomic map and the 1D concentration profile across the Cr layer obtained from APT measurement (Fig. 3(c)) demonstrate that Cr diffuses neither into the PtIr layer nor into the WC substrate. Around 10 at.% Ir and 8 at.% Pt are found to be segregated at the Cr/WC interface, indicating that during deposition, Ir and Pt rapidly diffused through the Cr layer, but their penetration into the WC substrate was restricted. There is also around 10 at.% W segregated at the Cr/WC interface, which may be attributed to the loss of carbon during the plasma activation prior to coating. Within the Cr layer, some small, dispersed Cr-oxide particles are found. Since Cr is a fairly active metal, it is difficult to achieve vacuum conditions inside the deposition chamber good enough to avoid its oxidation. Therefore, during sputter deposition, some Cr atoms will react with oxygen from the residual gas and form Cr oxides. The APT analyses of the WC substrate indicate that C and W atoms distribute homogeneously while Co, as the binder phase, is mainly segregated at WC grain boundaries (not shown).

3.1.2. After 6 h exposure at 630 °C under 1.12×10^{-23} bar O_2 partial pressure

Comparing the 6h-exposed state with the as-fabricated state, no obvious differences can be found between both surface SEM and cross-sectional STEM images (not shown here). The side view atom map of the Cr layer (Fig. 4(a)) also confirms that no massive diffusion took place. The PtIr coating, the Cr interlayer and the WC substrate are well separated. Both the PtIr/Cr and Cr/WC interfaces are still sharp and flat. However, as shown in Fig. 4(b), at the bottom of the PtIr layer, Cr is observed to segregate to several planar features, which are likely to be grain boundaries. However, the segregated amount is relatively limited (~1.5-3.5 at.% Cr) and around 30 nm away from the original Cr layer, no further segregation can be detected (Fig. 4(c)).

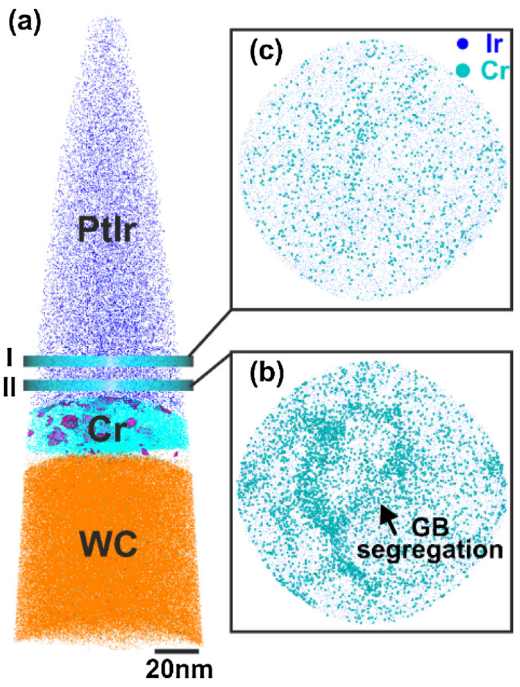

Fig. 4. 3D atom maps obtained from the near Cr layer region of the PtIr/Cr/WC specimen after 6 h exposure at 630 °C under 1.12×10^{-23} bar O_2 partial pressure: (a) Side view, (b) top view of the slice II marked in (a), and (c) top view of the slice I marked in (a). For clarity, only Ir (blue), Cr (cyan), O (magenta) and W ions (orange) are shown, if any of them are detected. (For interpretation of the references to colour in this figure legend, the reader is referred to the web version of this article.)

3.1.3. After 18 h exposure at 630 °C under 1.12×10^{-23} bar O_2 partial pressure

Fig. 5(a) is an SEM image acquired from the surface of the 18h-exposed specimen. Compared to the as-fabricated state (Fig. 3(a)), the surface morphology has changed. Fig. 5(b) is a BF STEM image obtained from a cross-sectional TEM lamella. Even though the Cr layer can still be distinguished, as indicated by the brightness change, its upper region seems to be dissolved, resulting in a wavy PtIr/Cr interface. However, the Cr/WC interface is still intact and flat. Fig. 6(a) shows a representative 3D atom map obtained from the Cr layer region and a corresponding magnified cross-sectional BF STEM image. To better illustrate the distribution of each species, blue-to-red rainbow colour concentration maps (blue indicates lowest concentration and red indicates highest concentration) are shown in Fig. 6(b) and a 1D concentration profile from the PtIr layer to the WC substrate is plotted in Fig. 6(c). Both the APT and STEM results reveal the formation of an ~50-nm-thick interdiffusion zone between the PtIr and Cr layer which exhibits an inhomogeneous chemical composition. The Cr content progressively decreases while the Ir content increases towards the PtIr layer. The Cr oxides formed during deposition can still be detected, which seems stable and remain immobile, thereby providing a marker of the position of the original Cr layer. As displayed in Fig. 6(c), this intermixed region is found to form on the basis of the outward diffusion of Cr. There are still some non-uniform, interrupted fragments of the Cr layer left near the Cr/WC interface. Fig. 7(a) and (b) are side and top view 3D atom maps obtained from the PtIr layer, respectively. Compared to the 6h-exposed state, larger amount of Cr (~2.6–5.9 at.% Cr) segregating at these grain-boundary-like-features. Fig. 8 shows a STEM-EDS map and a corresponding HAADF STEM image of a plan-view TEM lamella, from which the grain size and grain structure of the PtIr layer can be revealed. Since Cr is exclusively detected at grain boundaries, it can be confirmed that the features where Cr is seen to segregate in the APT datasets are

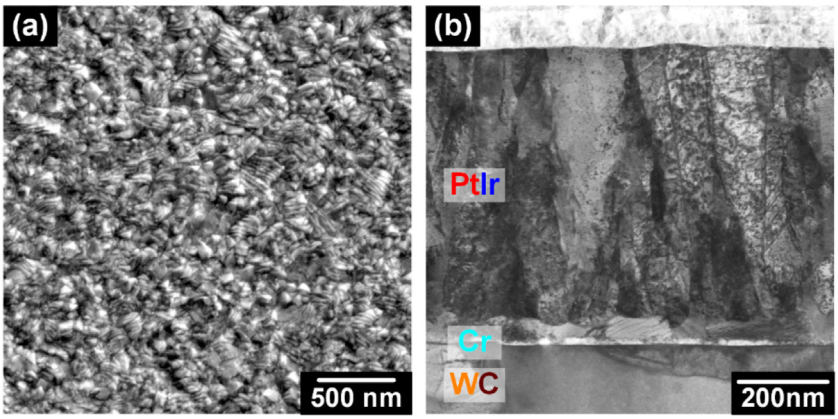

Fig. 5. Surface SEM (a) and cross-sectional BF STEM image (b) of the PtIr/Cr/WC specimen after 18 h exposure at 630 °C under 1.12×10^{-23} bar O_2 partial pressure.

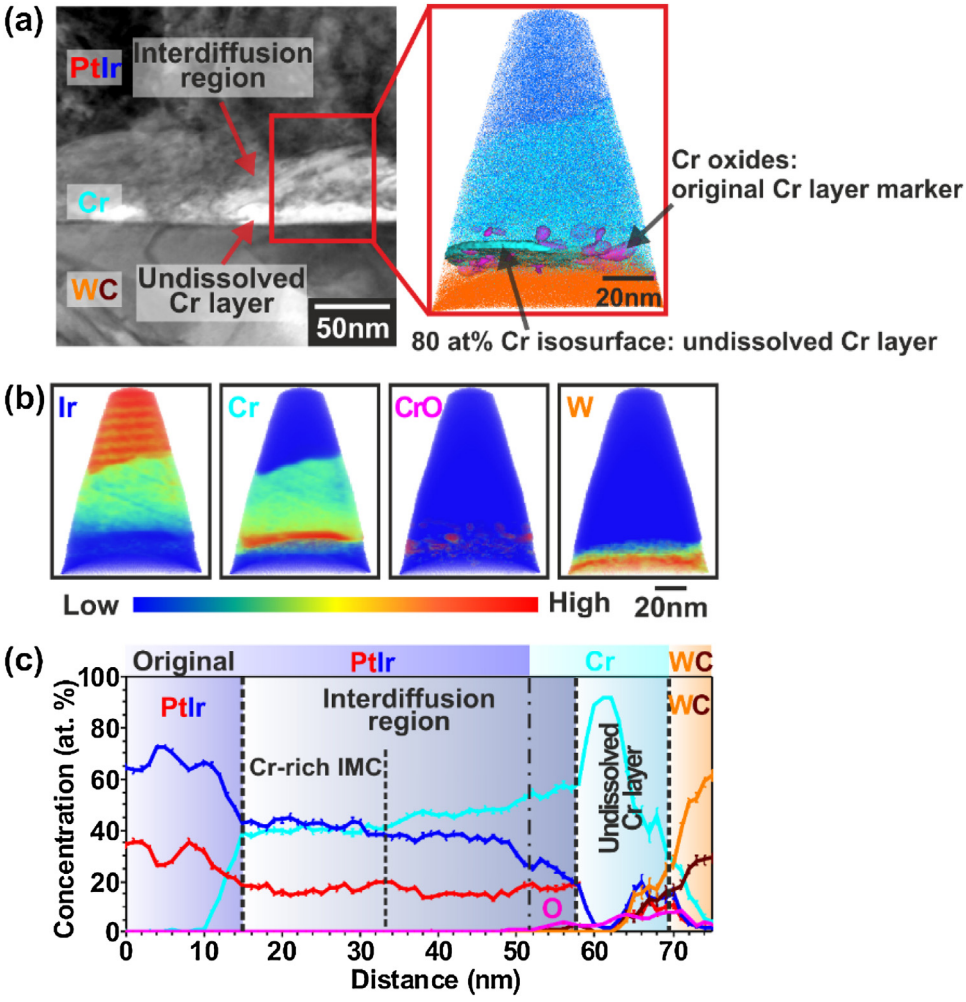

Fig. 6. Representative characterisation results obtained from the near Cr layer region of the PtIr/Cr/WC specimen after 18 h exposure at 630 °C under 1.12×10^{-23} bar O_2 partial pressure: (a) A 3D atom map together with a magnified cross-sectional BF STEM image; (b) corresponding blue-to-red rainbow colour concentration maps of Ir, Cr, CrO and W ions with the colour scale that blue indicates the lowest concentration and red indicates the highest concentration; (c) 1D concentration profile from the PtIr layer to the WC substrate. The interdiffusion region and undissolved Cr layer can be observed. For comparison, the original locations of the PtIr and Cr layers as well as the WC substrate are shown. At the diffusion front, the ~20-nm-thick layer with almost constant composition is supposed to be Cr-rich intermetallic compound (IMC). (For interpretation of the references to colour in this figure legend, the reader is referred to the web version of this article.)

actually grain boundaries. In fact, the segregation of Cr at PtIr grain boundaries gives evidence of the short circuit diffusion process. No noticeable amount of oxygen or any oxide particles are detected at the grain boundaries.

Fig. 9 shows the APT analysis result from the surface region. Here, discontinuous nanometre-sized Cr oxide islands are found. Fig. 9(b) illustrates top view blue-to-red rainbow colour concentration maps of Cr from different depth of the dataset shown in Fig. 9 (a). Blue colour indicates 0 at.% Cr and red indicates 3.5 at.%

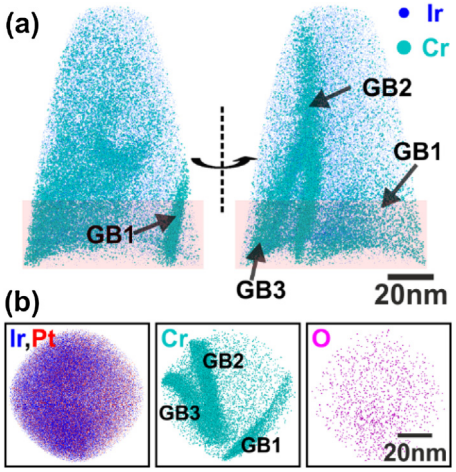

Fig. 7. 3D atom maps obtained from the PtIr layer of the PtIr/Cr/WC specimen after 18 h exposure at 630 °C under 1.12×10^{-23} bar O_2 partial pressure: (a) Side view (for clarity, Pt ions are not shown); (b) top view of the region marked by the semi-transparent cube in (a). Here Cr ions are denoted with bigger dots to highlight their segregation at grain boundaries.

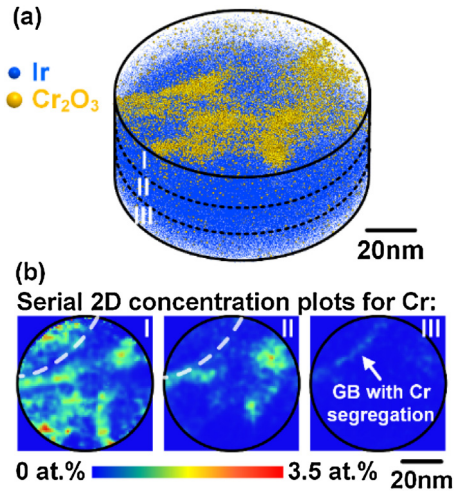

Fig. 9. (a) 3D atom map of the near surface region of the PtIr/Cr/WC specimen after 18 h exposure at 630 °C under 1.12×10^{-23} bar O_2 partial pressure. Tiny Cr oxides can be found on the surface. (b) Top view blue-to-red rainbow colour concentration maps of Cr from different depth of the dataset shown in (a), where blue indicates 0 at.% Cr and red indicates 3.5 at.% Cr. The white dashed lines in I and II depict the position of the grain boundary marked with the white arrow in III. (For interpretation of the references to colour in this figure legend, the reader is referred to the web version of this article.)

Cr. As marked by the white arrow (Fig. 9(b) III), underneath the surface, there is a grain boundary decorated with Cr atoms. The Cr atoms diffuse via PtIr grain boundaries and then get in contact with oxygen at the positions where grain boundaries intersect with the surface. However, as Fig. 9(b) I and II reveal, the nucleation of Cr oxides is not restricted to the grain boundary area (indicated by the white dashed lines), implying that metallic Cr atoms also diffused laterally on the surface before reacting with oxygen. Fig. 10(a) is a cross-sectional TEM image of the surface region at higher magnification, in which the thin brightest layer is considered to be the approximately 1-nm-thick Cr oxide. At this stage, the surface is not fully covered by Cr oxides. Fig. 10(b) shows the AES surface maps of Cr, Ir and Pt. Consistent with the APT and TEM observations, inhomogeneous Cr signals were detected. Since AES is a highly surface sensitive technique, the extensive Ir and Pt signals confirm that the surface Cr oxides are thinner than 2 nm.

3.1.4. After 168 h exposure at 630 °C under 1.12×10^{-23} bar O_2 partial pressure

Fig. 11(a) is an SEM picture taken from the surface of the 168h-exposed PtIr/Cr/WC specimen. Compared to the as-fabricated (Fig. 3(a)) and the 18h-exposed specimens (Fig. 5(a)), the 168h-exposed specimen exhibits a different surface morphology. The BF STEM image of a cross-sectional TEM lamella (Fig. 11(b)) shows that the original Cr layer has been completely dissolved and voids have formed. The Cr/WC interface also becomes rough. Another noticeable feature is the surface oxide scale, which can be seen more clearly in the magnified BF STEM image shown in Fig. 12(a). After 168 h, larger amounts of Cr atoms have reached the top surface and contributed to the development of a thicker oxide scale, which is identified to be Cr_2O_3 by AES (Fig. 12(b)). Besides these surface oxides, no other newly formed oxides nor any measurable amount of oxygen are detected inside the structure (Fig. 12(c)). In addition, unlike the 18h-exposed state, not only Cr atoms, but also W and Co atoms are found at grain boundaries and triple junctions of the PtIr layer, which is a strong indication that WC is, at this stage, also involved in the degradation process. Fig. 13 shows a magnified cross-sectional HAADF STEM image of the interfacial region together with representative APT results from this region: (b) the bottom part of the PtIr layer, (c) the PtIr/Cr interface, and (d) the Cr/WC interface. As mentioned above, the embedded small Cr-oxide particles can be used as a tracer of the original position of the Cr layer. Fig. 13 (d) illustrates that the remaining Cr is present only in a very limited amount. Non-uniform damage of the WC substrate occurs at the Cr/WC interface, where the degradation features

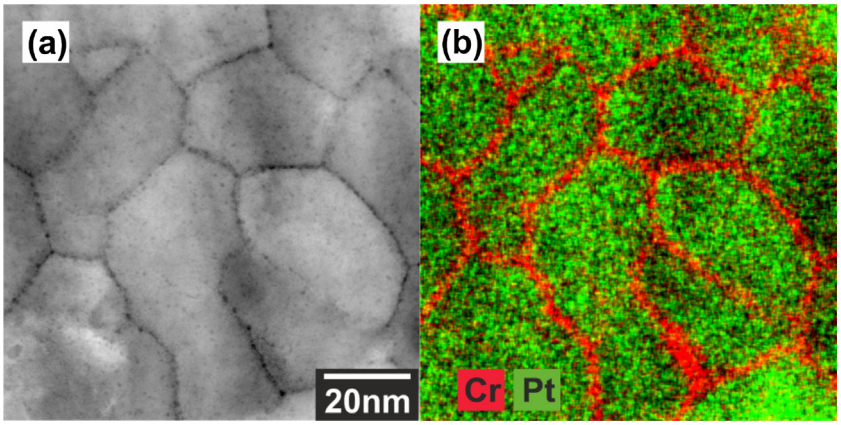

Fig. 8. (a) STEM HAADF image of a plan-view TEM lamella fabricated from the PtIr/Cr/WC specimen after 18 h exposure at 630 °C under 1.12×10^{-23} bar O_2 partial pressure. (b) The corresponding STEM-EDS map showing the distribution of Pt and Cr. The map clearly reveals the segregation of Cr to the PtIr grain boundaries.

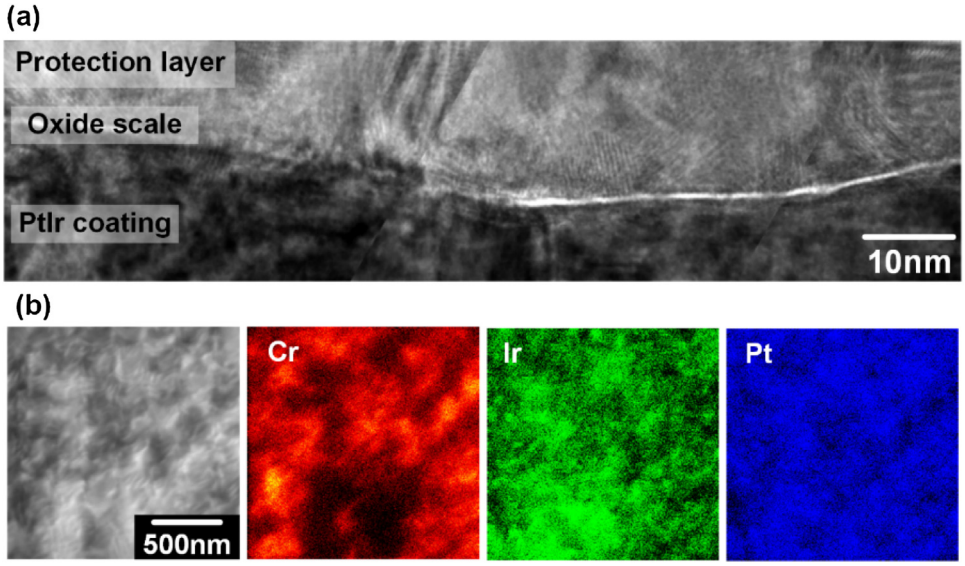

Fig. 10. (a) Magnified cross-sectional TEM image of the near surface region of the PtIr/Cr/WC specimen after 18 h exposure at 630 °C under 1.12×10^{-23} bar O_2 partial pressure. A thin, discontinuous surface oxide scale can be observed. (b) AES surface elemental maps showing the distribution of Cr, Ir and Pt respectively. In addition, the SEM image of the measured area is also shown.

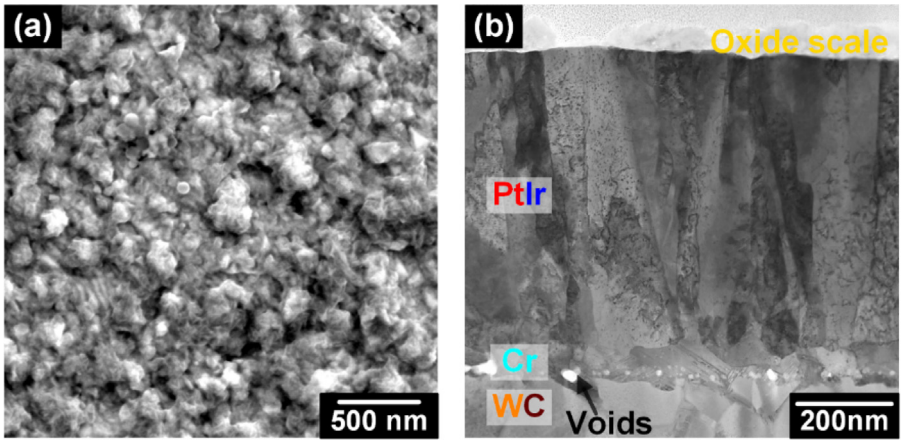

Fig. 11. Surface SEM (a) and cross-sectional BF STEM image (b) of the PtIr/Cr/WC specimen after 168 h exposure at 630 °C under 1.12×10^{-23} bar O_2 partial pressure.

along grain boundaries are severe. The interdiffusion zone formed between PtIr and Cr after 18 h exposure evolved further into a mixture of small Cr-rich and W-rich regions (Fig. 13(b)). Additionally, in the bottom part of the PtIr layer, some Cr-rich particles are found at the grain boundaries and W atoms segregate at the particle/matrix interfaces.

3.2. PtIr/Ni/WC specimen

The surface SEM and cross-sectional STEM images (not shown here) of the as-fabricated PtIr/Ni/WC specimen reveal similar features as the microstructure of the as-fabricated PtIr/Cr/WC specimen. The three different regions, PtIr layer, Ni layer and WC substrate can be clearly distinguished and both PtIr/Ni and Ni/WC interfaces are flat, sharp and free of voids. However, as illustrated in Fig. 14, some differences were discovered by APT analysis. Firstly, there are no embedded Ni oxides within the Ni layer, which can be attributed to the higher oxidation resistance of Ni compared to Cr. Secondly, even in the as-fabricated state, outward diffusion of Ni along PtIr grain boundaries has already taken place, but the extent is small and the diffusion length is below 50 nm.

Fig. 15 summarises the representative characterisation results of the PtIr/Ni/WC specimen after 48 h exposure at 630 °C under 1.12×10^{-23} bar O_2 partial pressure. The cross-sectional BF STEM image (Fig. 15(a)) shows that the PtIr/Ni interface is blurred and the original Ni layer seems to already disappear. Fig. 15(b) exhibits the APT result obtained from the near surface region of the specimen. Ni atoms rather than Ni oxides are found to accumulate at the surface. Within the PtIr layer, the enrichment of Ni atoms at grain boundaries is obvious (Fig. 15(c)), revealing that the outward diffusion of Ni is also supported by the short circuit diffusion mechanism. The 1D concentration profile across the grain boundary (Fig. 15(c)) indicates that at this stage, only Ni atoms are segregated at the grain boundaries. Fig. 15(d) summarises the results obtained from APT analysis of the near Ni layer region. Similar to the PtIr/Cr/WC sample, an interdiffusion region formed, which contains Ni-rich and W-rich zones. Even though from the cross-sectional STEM image, no obvious damages are visible at the Ni/WC interface, the APT results clearly suggest that the degradation of WC already started. However at such relatively short exposure time, elements from the WC substrate have not yet penetrated into the PtIr layer.

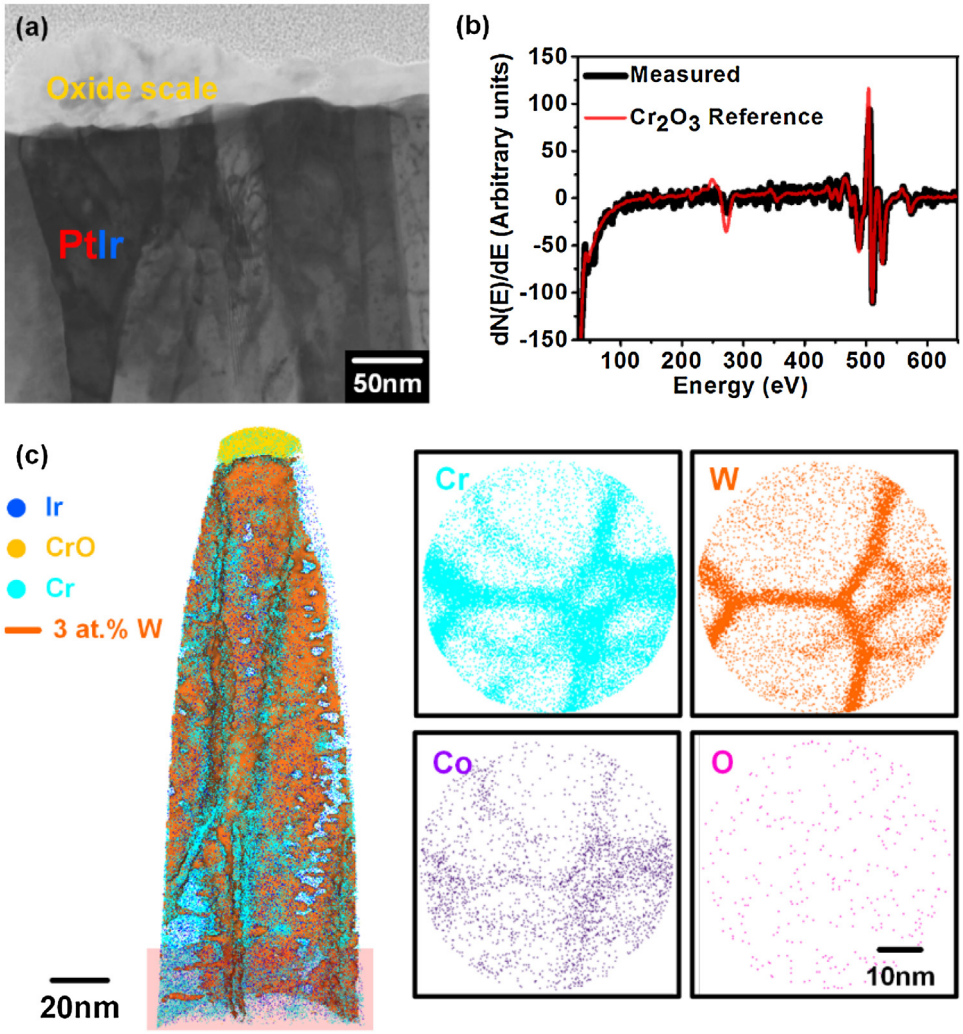

Fig. 12. Representative characterisation results obtained from the near surface region of the PtIr/Cr/WC specimen after 168 h exposure at 630 °C under 1.12×10^{-23} bar O_2 partial pressure: (a) cross-sectional BF STEM image; (b) AES point analysis result (differential spectrum) showing that the surface oxides are Cr_2O_3; (c) 3D atom maps. Left: side view; right: top view of the bottom 30 nm slice of the dataset shown on the left, as marked by the semi-transparent cube. The segregation of Cr, W and Co atoms at the PtIr grain boundaries are detected.

4. Discussion

The degradation evolution in the PtIr/Cr/WC specimen deduced from the experimental observations is sketched in Fig. 16. Similar phenomena were observed in the case of the PtIr/Ni/WC specimen. The only major difference is that when Ni atoms diffuse through the PtIr layer and reach the surface, they are not oxidised. According to thermodynamics, see e.g. the Ellingham diagram [46], at 630 °C, the critical oxygen partial pressure to oxidise Ni is $\sim 10^{-17}$ bar, which is substantially higher than the one applied in our experiments ($\sim 1.12 \times 10^{-23}$ bar).

4.1. Outward diffusion of the interlayer

The outward transport and segregation of Cr or Ni atoms along the grain boundaries of the PtIr layer seems to indicate the onset of the degradation process. For the PtIr/Cr/WC specimen, these processes take place slowly at the beginning. After 6 h exposure, only a small amount of Cr is detected at the PtIr grain boundaries, within a diffusion distance of approximately 30 nm. Compared to Cr, Ni follows the same transport mechanism but at a higher diffusion rate. Already during coating deposition, Ni atoms penetrate into the PtIr layer. From a thermodynamic point of view, the gradient in chemical potentials or activities of individual elements across the interface drives their diffusion. This gradient in chemical potential, together with the elemental diffusivity, determines their diffusion behaviour. Typically, diffusion along grain boundaries is 4–8 orders of magnitude faster than transport within grain interiors [47], therefore, at relatively short time and low temperature (type B-diffusion regime [48,49]), grain boundaries are the main pathways for the outward diffusion of atoms from the interlayer. Grain boundary diffusion data for Cr and Ni in PtIr are not available in literature. According to our results of the as-fabricated and early degradation states, it is likely that Ni diffuses faster than Cr. However, after 48 h, as shown in Fig. 17, the whole surface of the PtIr/Cr/WC sample is covered by an oxide scale with a thickness in the range of 15–120 nm. While for the PtIr/Ni/WC sample, even after 48 h, the quantity of Ni atoms accumulating on the surface is still small (Fig. 15(a)), which seems to contradict our previous inference that Ni diffuses more rapidly than Cr. It has been reported in previous studies that surface oxidation can strongly affect internal material transport. The first diffusion step of solutes decorating the PtIr grain boundaries is driven by the Gibbs adsorption isotherm, i.e. the interface energy gets reduced by solute decoration. This creates a diffusion flux along the grain boundaries towards the surface. As the diffusing species reach the film surface, the oxidation process

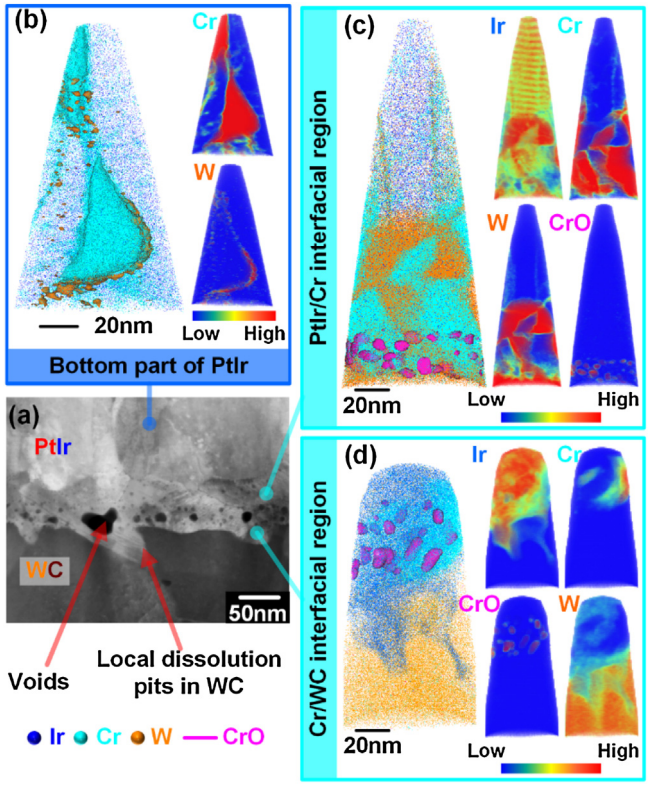

Fig. 13. Representative characterisation results obtained from the near interface region of the PtIr/Cr/WC specimen after 168 h exposure at 630 °C under 1.12×10^{-23} bar O_2 partial pressure: (a) cross-sectional HAADF STEM image. (b) On the left: 3D atom map of the bottom part of the PtIr layer with iso-concentration surface of 1.2 at.% W (orange); on the right: corresponding blue-to-red rainbow colour concentration maps of Cr and W. (c) On the left: 3D atom map of the PtIr/Cr interfacial region; on the right: corresponding blue-to-red rainbow colour concentration maps of Ir, Cr, W and CrO. (d) On the left: 3D atom map of the Cr/WC interfacial region; on the right: corresponding blue-to-red rainbow colour concentration map of Ir, Cr, CrO and W. In all concentration maps, blue indicates the lowest concentration and red indicates the highest concentration. For clarity, in all atom maps, only Ir (blue), Cr (cyan), W (orange) ions and Cr oxide particles (magenta) are shown, if any of them are detected. (For interpretation of the references to colour in this figure legend, the reader is referred to the web version of this article.)

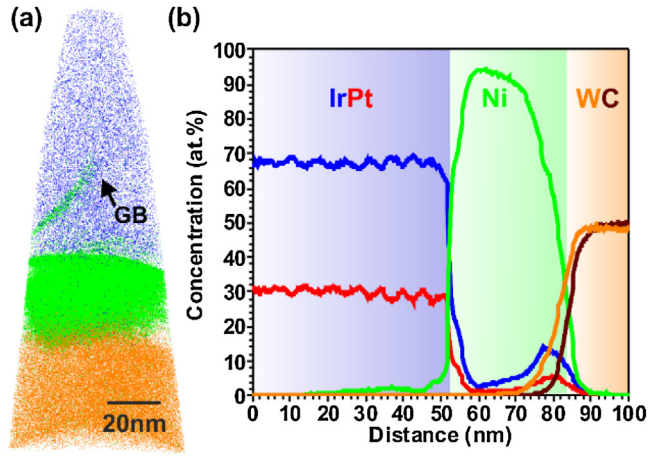

Fig. 14. (a) 3D atom map of the near Ni layer region of the as-fabricated PtIr/Ni/WC specimen. For clarity, only Ir (blue), Ni (green) and W (orange) ions are shown. (b) 1D concentration profile across the Ni layer. (For interpretation of the references to colour in this figure legend, the reader is referred to the web version of this article.)

starts removing solutes from the material, particularly from the decorated grain boundaries because they get trapped in the oxides. This effect reduces their solute chemical potential on the grain boundaries, hence creating a chemical potential gradient towards the surface, promoting further outbound diffusion [31,50–54]. Then the outward transportation of the diffusing element becomes the slower, rate-controlling step [55]. As for the PtIr/Ni/WC sample, the exposure atmosphere is non-oxidising. There is no substantial attractive force to further promote the spreading and lateral diffusion of Ni atoms onto the PtIr surface, especially once a first surface coverage is reached. Under such conditions, Ni atoms will be mostly trapped along the grain boundaries of the PtIr layer. Therefore, as illustrated in Fig. 15 (c), significant enrichments of Ni (~30 at.%) with broad segregation zones (>10 nm) are frequently found at numerous PtIr grain boundaries. When they are saturated, there will be no further thermodynamic driving force for further segregation.

4.2. Formation of intermetallic phase and evolution of the interfacial region

Since there is no substantial difference in the internal degradation processes between the PtIr/Cr/WC and the PtIr/Ni/WC specimen, in this and the following subsections, the PtIr/Cr/WC system will be taken as representative. After 168 h exposure at 630 °C under 1.12×10^{-23} bar O_2 partial pressure, Cr-rich particles appear at PtIr grain boundaries (Fig. 13(b)) as well as inside the interdiffusion region (Fig. 13(c)). APT analysis reveals that the chemical compositions of all these Cr-rich particles are similar, namely approximately 56 at.% Ir, 17 at.% Pt and 27 at.% Cr. Studies about the Pt-Ir-Cr ternary system are rare in the literature and knowing the chemical composition of the precipitates alone is insufficient to draw an unequivocal conclusion about the associated reaction and phase transformation pathways. The compositional similarity observed is nonetheless a strong indication that all these particles belong to the same type of intermetallic phase. Moreover, after 168 h exposure, local equilibria between PtIr and the newly formed intermetallic compound particles are most likely established, which means that this intermetallic phase, denoted here as $(Pt,Ir)_3Cr$, is the first stable intermetallic phase from the PtIr-rich side to the Cr-rich side, yet, with comparably high PtIr content and low Cr content. After 18 h, volume diffusion induced changes become substantial. A well-defined interdiffusion zone between the PtIr and Cr layer appears (Fig. 6) and Cr is proven to be the dominant diffusing species. However, surprisingly, the Cr content within the whole region is much higher than 27 at.%. Additionally, as noted from the concentration profile, in the diffusion front, there is an ~20-nm-thick thin layer with almost constant composition (marked in Fig. 6(c)), namely approximately 43 at.% Ir, 17 at.% Pt and 40 at.% Cr. It is thus very likely that another type of intermetallic phase has formed, denoted here as $(Pt,Ir)_3Cr_2$, which should be closer to the Cr-rich side in the phase diagram.

The evolution from the Cr-rich to the PtIr-rich intermetallic compound can be explained by the following mechanism. Firstly, the intermetallic phase with the lowest effective interfacial reaction barrier, e.g. $(Pt,Ir)_3Cr_2$, nucleates at the PtIr/Cr interface. With ongoing exposure, the Cr interlayer is continuously consumed by the growth of these intermetallic compound nuclei as well as the formation of surface oxide scale. When the original Cr layer has been fully consumed, the Cr activity will drop and the formation of $(Pt,Ir)_3Cr_2$ will stop. Subsequently, the chemical potential gradient across the PtIr/$(Pt,Ir)_3Cr_2$ interface will drive PtIr to diffuse into $(Pt,Ir)_3Cr_2$ and Cr may diffuse out. After a short transition period, the second intermetallic phase, i.e. $(Pt,Ir)_3Cr$, with higher PtIr content will form and grow. Correspondingly, $(Pt,Ir)_3Cr_2$ will shrink and even disappear. This phenomenon, termed as supply limita-

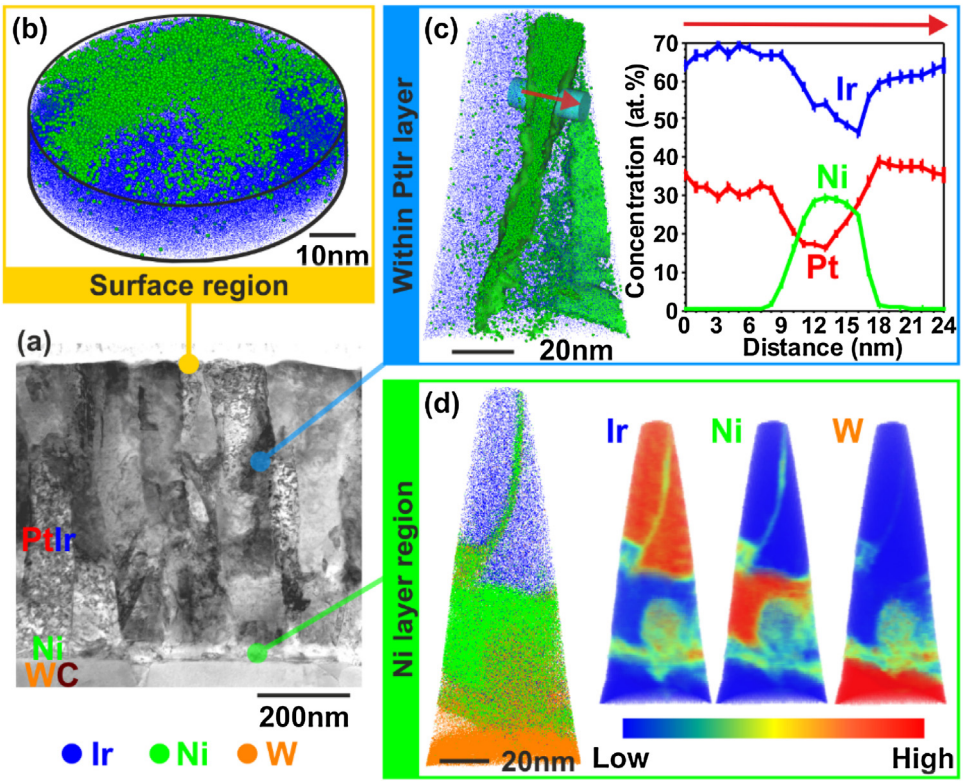

Fig. 15. Representative analysis results obtained from the PtIr/Ni/WC specimen after 48 h exposure at 630 °C under 1.12×10^{-23} bar O_2 partial pressure: (a) cross-sectional BF STEM image. (b) 3D atom map of the surface region. (c) On the left: 3D atom map of the PtIr layer with iso-concentration surface of 15 at.% Ni (green); on the right: 1D concentration profile within the cylinder highlighted in the atom map along the direction marked with the red arrow. (d) on the left: 3D atom map of the near Ni layer region; on the right: corresponding blue-to-red rainbow colour concentration maps of Ir, Ni, and W with the colour scale that blue indicates the lowest concentration and red indicates the highest concentration. For clarity, in all atom maps, only Ir (blue), Ni (green) and W (orange) ions are shown, if any of them are detected. (For interpretation of the references to colour in this figure legend, the reader is referred to the web version of this article.)

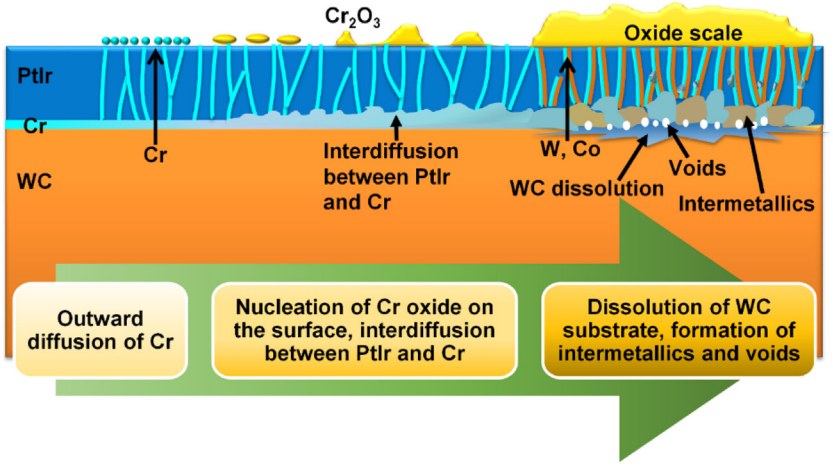

Fig. 16. Schematic illustration of the evolution of degradation of the PtIr/Cr/WC system during isothermal exposure at 630 °C under a well-controlled atmosphere (N_2-2.5%H_2 with +20 °C dew point, $P_{O2} \approx 1.12 \times 10^{-23}$ bar).

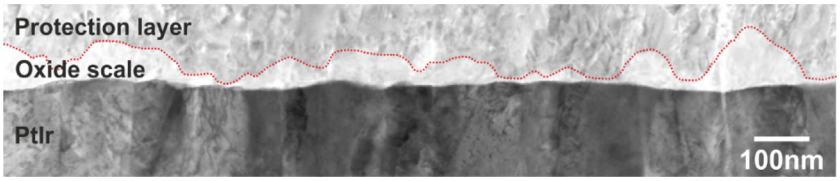

Fig. 17. Cross-sectional BF STEM image of the near surface region of the PtIr/Cr/WC specimen after 48 h exposure at 630 °C under 1.12×10^{-23} bar O_2 partial pressure. The edge of the surface oxide scale is highlighted using red dotted line. (For interpretation of the references to colour in this figure legend, the reader is referred to the web version of this article.)

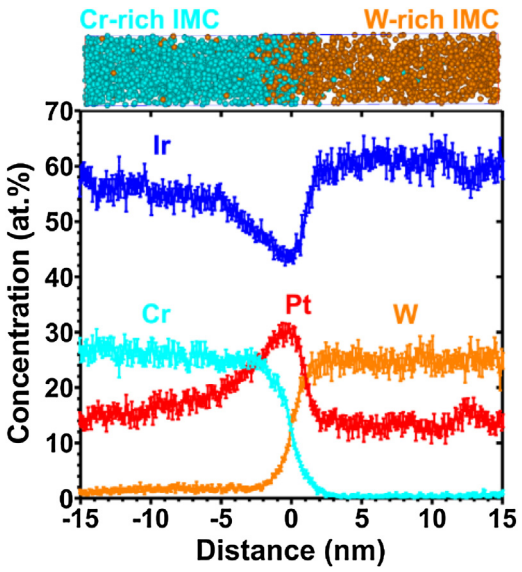

Fig. 18. APT resulted 1D concentration profile and a corresponding atom map across the interface between a Cr-rich and a W-rich intermetallic compound (IMC). For clarity, only Cr (cyan) and W ions (orange) are shown. (For interpretation of the references to colour in this figure legend, the reader is referred to the web version of this article.)

tion induced second phase formation, has been reported in various previous studies [11,56–63].

At a later stage, the WC substrate also gets involved in the reactive interdiffusion process, giving rise to the formation of a W-rich intermetallic compound (Fig. 13). Fig. 18 shows a 1D concentration profile from a Cr-rich to a W-rich particle. The solubility of Cr in the W-rich particles is found to be very limited, implying that Cr atoms have been substituted by W atoms to form a W-rich phase. Actually, the Cr-rich intermetallic phase is the product of the reaction between PtIr and Cr layer. After the full consumption of the Cr layer, WC becomes the new endmember. For this system, i.e. PtIr-WC, the Cr-rich intermetallics should be unstable phases, which will be gradually replaced by thermodynamically more stable phases, such as the observed W-rich phase. In addition to the intermetallic compounds, a chain of nanometre-sized voids are also formed in the interfacial region (Fig. 13). This phenomenon is attributed to the Kirkendall effect, where an imbalance in mass transport due to different diffusion rates creates free volume and hence voids are formed. More specific, in the present case where Cr is the dominating diffusing species, during its outward diffusion, vacancies move in the opposite direction. These extra vacancies may condensate further into voids [9,64–66], which may play an important role in the onset of degradation of the WC substrate.

4.3. Dissolution of the tungsten carbide

The dissolution of WC occurring during the later stages of degradation first requires the decomposition of the compound, especially considering that only W atoms, rather than WC entities, were involved in the reactive interdiffusion process. Since no C atoms were found within the surface coating, a possibility is that WC first reacted with oxygen, resulting in elemental tungsten as well as gaseous species such as CO and CO_2, which formed at the expense of the free carbon atoms, and finally leaked into the atmosphere [67,68]. As for the material we studied here, WC has no direct contact with air, the pre-requisite is that oxygen penetrate through the coating. However according to the APT results, no substantial amounts of oxygen were detected (Fig. 7 (b), Fig. 12 (c)). A possible reason could be that after exposure, specimens are cooled down to room temperature slowly (cooling rate ~5 °C/min). During such a slow cooling procedure, gases including O_2, CO and CO_2 may escape for instance via diffusing along the grain boundaries. Another possibility is that these gaseous phases may be trapped in the observed voids at the interfacial region and promote further void nucleation and growth [69,70].

APT relies on the detection of individual ions which are successively field evaporated from a sharp, needle-shaped specimen and identification of them using time-of-flight (TOF) mass spectrometry. Quantitative chemical information is normally obtained through counting the ions within the peaks of the resulting mass spectrum, which is a histogram showing the number of the detected ions as a function of mass-to-charge ratio, i.e. TOF value [71–73]. Therefore, the accuracy of the results will be influenced by errors for example in peak recognition, peak deconvolution, mass ranging and background subtraction [74,75]. In some cases, minor peaks may be buried under background due to their low intensity. In this study, the possible important simple or molecular ion species that contain oxygen are O^+, O_2^+, CrO^{2+}, CrO^+, CrO_2^{2+}, CrO_2^+ and CrO_3^+. The overall noise level at these positions is evaluated to fall into the range of 0.18–0.84 at.%, depending on the data set. Therefore, if the oxygen content is below ~1 at.%, it would not necessarily be properly quantified. Indeed, since Cr is not found to be oxidised internally at least up to this stage, the activity of oxygen within the material interior should be below the critical partial pressure of Cr oxidation. According to the Ellingham diagram, at 630 °C, the critical oxygen partial pressure for Cr oxidation is $\sim 10^{-34}$ bar ($Cr \rightarrow Cr_2O_3$), and for W oxidation is $\sim 2.2 \times 10^{-25}$ bar ($W \rightarrow WO_2$) [46]. If Cr has not been oxidised internally, it is not possible for W to get oxidised. However, if coating spallation takes place, and the WC substrate is in direct contact with air, or in case that the metallic tungsten atoms diffuse to the surface, where higher oxygen partial pressure prevails, oxidation of tungsten will take place.

5. Conclusion

We investigated the stability and degradation evolution of a bimetallic layer coating (PtIr/Cr and PtIr/Ni) on cemented tungsten carbide substrate during isothermal exposure treatment at 630 °C under a well-controlled atmosphere (N_2-2.5%H_2 with +20 °C dew point, $P_{O2} \approx 1.12 \times 10^{-23}$ bar). From our experimental results, the following conclusions can be drawn:

(1) The transport and migration of different atomic species can be traced by APT. Combining the APT results with detailed microstructure analysis using advanced electron microscopy such as STEM provides additionally new insights into the degradation process in multilayer thin films or coatings.
(2) Both systems studied, i.e. PtIr/Cr/WC and PtIr/Ni/WC, are unstable under the exposure conditions. Cr or Ni were observed to diffuse through PtIr grain boundaries to the surface, where Cr got oxidised selectively, while Ni remained metallic. Internally, all three regions, i.e. PtIr, Cr (Ni) and WC, were involved in complex reactive interdiffusion processes, giving rise to intermetallic particles and voids at the interfacial region.
(3) The nanocrystalline columnar grain structure of the PtIr coating is a key factor limiting the stability of the system, as it provides numerous fast and short diffusion pathways.
(4) By comparing the PtIr/Cr/WC to the PtIr/Ni/WC samples, it is possible to infer that surface oxidation promotes the replenishing diffusion of solute Cr towards surface at the later exposure stages. Initially, for both systems, segregation to the grain boundaries is the dominating driving force for the outward diffusion, which occurs faster for Ni than for Cr.

Acknowledgements

The authors are grateful for the financial support from the InitialWear project, funded by the Max-Planck-Gesellschaft (MPG) and the Fraunhofer-Gesellschaft. The exposure treatments and AES measurements were conducted by Alexandra Vogel, we greatly appreciate her help. The authors are thankful to Uwe Tezins & Andreas Sturm for their support of the APT & FIB facilities at MPIE. Aleksander Kostka (Ruhr-Universität Bochum), Minjie Lai, Volker Kree and Christian Liebscher are thanked for their vital help in (S)TEM experiments.

References

[1] G.S. Upadhyaya, Cemented Tungsten, Carbides: Production Properties and Testing, Noyes Publications Westwood, New U.S.A. Jersey, 1998.
[2] Diffusion Phenomena in Thin Films and Microelectronic Materials, in: D. Gupta, P.S. Ho (Eds.), Noyes Publications, Park Ridge, New Jersey, USA, 1988.
[3] Thin Film Structures in Energy Applications, in: S. Babu Krishna Moorthy (Ed.), Springer International Publishing, Switzerland, 2015.
[4] K.L. Chopra, S.R. Das, Thin Film Solar Cells, Springer, New U.S.A. York, 1983.
[5] J.J. Yang, J.P. Strachan, Q. Xia, D.A.A. Ohlberg, P.J. Kuekes, R.D. Kelley, W.F. Stickle, D.R. Stewart, G. Medeiros-Ribeiro, R.S. Williams, Diffusion of adhesion layer metals controls nanoscale memristive switching, Adv. Mater. 22 (2010) 4034–4038.
[6] K.W. Vogt, P.A. Kohl, W.B. Carter, R.A. Bell, L.A. Bottomley, Characterization of thin titanium oxide adhesion layers on gold: resistivity, morphology, and composition, Surf. Sci. 301 (1994) 203–213.
[7] H. Hieber, Aging properties of gold layers with different adhesion layers, Thin Solid Films 37 (1976) 335–343.
[8] G. Bernhardt, C. Silvestre, N. LeCursi, S.C. Moulzolf, D.J. Frankel, R.J. Lad, Performance of Zr and Ti adhesion layers for bonding of platinum metallization to sapphire substrates, Sens. Actuators B Chem. 77 (2001) 368–374.
[9] K. Zeng, R. Stierman, T.-C. Chiu, D. Edwards, K. Ano, K.N. Tu, Kirkendall void formation in eutectic SnPb solder joints on bare Cu and its effect on joint reliability, J. Appl. Phys. 97 (2005) 24508.
[10] J. Li, A. Dasgupta, Failure mechanism models for material aging due to interdiffusion, IEEE Trans. Reliab. 43 (1994) 2–10.
[11] Thin Films: Interdiffusion and Reactions, in: J.M. Poate, K. Tu, J.W. Mayer (Eds.), John Wiley & Sons, New York, USA, 1978.
[12] M. Ohring, Materials Science of Thin Films, 2nd ed., Academic Press, Orlando, USA, 2001.
[13] K.J. Ma, H.H. Chien, W.H. Chuan, C.L. Chao, K.C. Hwang, Design of protective coatings for glass lens molding, Key Eng. Mater. 364–366 (2008) 655–661.
[14] K. Bobzin, N. Bagcivan, T. Brögelmann, T. Münstermann, Correlation between chemical glass components and the glass sticking on sputtered PtIr physical vapour deposition coatings for precision blank moulding, Mater. Sci. Appl. 5 (2014) 316–329.
[15] K. Bobzin, N. Bagcivan, M. Ewering, R.H. Brugnara, T. Münstermann, Influence of interlayer thickness of a thin noble metal MSIP-PVD coating on compound and system properties for glass lens moulding, Prod. Eng. 6 (2012) 311–318.
[16] F. Klocke, O. Dambon, A.Y. Yi, F. Wang, M. Hünten, K. Georgiadis, D. Hollstegge, J. Dukwen, Process chain for the replication of complex optical glass components, in: E. Brinksmeier, O. Riemer, R.M. Gläbe (Eds.), Fabr. Complex Opt. Components From Mold Des. to Prod., Springer, Berlin Heidelberg, 2013, pp. 119–132.
[17] A.Y. Yi, A. Jain, Compression molding of aspherical glass lenses-A combined experimental and numerical analysis, J. Am. Ceram. Soc. 88 (2005) 579–586.
[18] L. Zhang, W. Liu, Precision glass molding: toward an optimal fabrication of optical lenses, Front. Mech. Eng (2016) 1–15.
[19] H. Monji, M. Aoki, H. Torii, H. Okinaka, Mold for Press-molding Glass Elements, United States Patent No. 4 721 518, 1988.
[20] F. Klocke, K.-D. Bouzakis, K. Georgiadis, S. Gerardis, G. Skordaris, M. Pappa, Adhesive interlayers' effect on the entire structure strength of glass molding tools' Pt–Ir coatings by nano-tests determined, Surf. Coat. Technol. 206 (2011) 1867–1872.
[21] F. Bernhardt, K. Georgiadis, O. Dambon, F. Klocke, Novel testing facility for investigating wear on PGM sample tools, in: J.L. Bentley, M. Pfaff (Eds.), Proc. SPIE (2013) (p. 88841 V).
[22] K.D. Fischbach, K. Georgiadis, F. Wang, O. Dambon, F. Klocke, Y. Chen, A.Y. Yi, Investigation of the effects of process parameters on the glass-to-mold sticking force during precision glass molding, Surf. Coat. Technol. 205 (2010) 312–319.
[23] F. Klocke, O. Dambon, M. Rohwerder, F. Bernhardt, M. Friedrichs, S.V. Merzlikin, Model of coating wear degradation in precision glass molding, Int. J. Adv. Manuf. Technol. 87 (2016) 43–49.
[24] K.N. Tu, Interdiffusion and reaction in bimetallic Cu-Sn thin films, Acta Metall. 21 (1973) 347–354.
[25] B. Yan, T. Lin, D. Mao, C. Yang, Interdiffusion of an Au/Ni/Cr multilayer metallization on silicon substrates, Thin Solid Films 173 (1989) 39–51.
[26] K. Holloway, P.M. Fryer, C. Cabral, J.M.E. Harper, P.J. Bailey, K.H. Kelleher, Tantalum as a diffusion barrier between copper and silicon: failure mechanism and effect of nitrogen additions, J. Appl. Phys. 71 (1992) 5433.
[27] J. Nazon, P. Simon, B. Domenichini, S. Bourgeois, Thermal stability under air of tungsten–titanium diffusion barrier layer between silica and platinum, Corros. Sci. 78 (2014) 208–214.
[28] Y.-I. Chen, L.-C. Chang, J.-W. Lee, C.-H. Lin, Annealing and oxidation study of Mo?Ru hard coatings on tungsten carbide, Thin Solid Films 518 (2009) 194–200.
[29] J. Masuda, J. Yan, T. Zhou, T. Kuriyagawa, Y. Fukase, Thermally induced atomic diffusion at the interface between release agent coating and mould substrate in a glass moulding press, J. Phys. D. Appl. Phys. 44 (2011) 215302.
[30] A.I. Oleshkevych, S.M. Voloshko, S.I. Sidorenko, G.A. Langer, D.L. Beke, A.R. Rennie, Enhanced diffusion caused by surface reactions in thin films of Sn–Cu–Mn, Thin Solid Films 550 (2014) 723–731.
[31] J.M. Poate, P.A. Turner, W.J. DeBonte, J. Yahalom, Thin-film interdiffusion. I. Au-Pd, Pd-Au, Ti-Pd, Ti-Au, Ti-Pd-Au, and Ti-Au-Pd, J. Appl. Phys. 46 (1975) 4275.
[32] R.N. Singh, Interdiffusion and compound formation in the Mo/Pd/Si thin film metallization system, Thin Solid Films 143 (1986) 249–257.
[33] I. Povstugar, P.-P. Choi, D. Tytko, J.-P. Ahn, D. Raabe, Interface-directed spinodal decomposition in TiAlN/CrN multilayer hard coatings studied by atom probe tomography, Acta Mater. 61 (2013) 7534–7542.
[34] D. Tytko, P.-P. Choi, D. Raabe, Thermal dissolution mechanisms of AlN/CrN hard coating superlattices studied by atom probe tomography and transmission electron microscopy, Acta Mater. 85 (2015) 32–41.
[35] P.-P. Choi, I. Povstugar, J.-P. Ahn, A. Kostka, D. Raabe, Thermal stability of TiAlN/CrN multilayer coatings studied by atom probe tomography, Ultramicroscopy 111 (2011) 518–523.
[36] T. Schwarz, O. Cojocaru-Mirédin, P. Choi, M. Mousel, A. Redinger, S. Siebentritt, D. Raabe, Atom probe tomography study of internal interfaces in Cu2ZnSnSe4 thin-films, J. Appl. Phys. 118 (2015) 95302.
[37] C.B. Ene, G. Schmitz, R. Kirchheim, A. Hütten, Stability and thermal reaction of GMR NiFe/Cu thin films, Acta Mater. 53 (2005) 3383–3393.
[38] M.R. Chellali, Z. Balogh, H. Bouchikhaoui, R. Schlesiger, P. Stender, L. Zheng, G. Schmitz, Triple junction transport and the impact of grain boundary width in nanocrystalline Cu, Nano Lett. 12 (2012) 3448–3454.
[39] M. Auinger, D. Vogel, A. Vogel, M. Spiegel, M. Rohwerder, A novel laboratory set-up for investigating surface and interface reactions during short term annealing cycles at high temperatures, Rev. Sci. Instrum. 84 (2013) 85108.
[40] G.B. Thompson, M.K. Miller, H.L. Fraser, Some aspects of atom probe specimen preparation and analysis of thin film materials, Ultramicroscopy 100 (2004) 25–34.
[41] M. Schaffer, B. Schaffer, Q. Ramasse, Sample preparation for atomic-resolution STEM at low voltages by FIB, Ultramicroscopy 114 (2012) 62–71.
[42] Z. Peng, P.-P. Choi, B. Gault, D. Raabe, Evaluation of analysis conditions for laser-pulsed atom probe tomography: example of cemented tungsten carbide, Microsc. Microanal. (2017) (pp. 1–12).
[43] M. Hans, M. to Baben, Y.-T. Chen, K.G. Pradeep, D.M. Holzapfel, D. Primetzhofer, D. Kurapov, J. Ramm, M. Arndt, H. Rudigier, J.M. Schneider, Substrate rotation-induced chemical modulation in Ti-Al-O-N coatings synthesized by cathodic arc in an industrial deposition plant, Surf. Coat. Technol. 305 (2016) 249–253.
[44] A.O. Eriksson, J.Q. Zhu, N. Ghafoor, M.P. Johansson, J. Sjölen, J. Jensen, M. Odén, L. Hultman, J. Rosén, Layer formation by resputtering in Ti–Si–C hard coatings during large scale cathodic arc deposition, Surf. Coat. Technol. 205 (2011) 3923–3930.
[45] L. Rogström, L.J.S. Johnson, M.P. Johansson, M. Ahlgren, L. Hultman, M. Odén, Age hardening in arc-evaporated ZrAlN thin films, Scripta Mater. 62 (2010) 739–741.
[46] N. Birks, G.H. Meier, F.S. Pettit, Introduction to the High Temperature Oxidation of Metals, 2nd ed., 2006.
[47] A.M. Brown, M.F. Ashby, Correlations for diffusion constants, Acta Metall. 28 (1980) 1085–1101.
[48] L.G. Harrison, Influence of dislocations on diffusion kinetics in solids with particular reference to the alkali halides, Trans. Faraday Soc. 57 (1961) 1191.
[49] H. Mehrer, Diffusion in Solids: Fundamentals, Methods, Materials, Diffusion-Controlled Processes, Springer, Berlin, 2007.
[50] H.G. Tompkins, M.R. Pinnel, Low-temperature diffusion of copper through gold, J. Appl. Phys. 47 (1976) 3804.
[51] C.-A. Chang, Effect of CO on the low temperature diffusion of Cr and Si through thin gold films, J. Electrochem. Soc. 127 (1980) 1331.
[52] J.H. Lee, H.D. Jeong, C.S. Yoon, C.K. Kim, B.G. Park, T.D. Lee, Interdiffusion in antiferromagnetic/ferromagnetic exchange coupled NiFe/IrMn/CoFe multilayer, J. Appl. Phys. 91 (2002) 1431.
[53] J.R. Rairden, C.A. Neugebauer, R.A. Sigsbee, Interdiffusion in thin conductor films – chromium/gold, nickel/gold and chromium silicide/gold, Metall. Trans. 2 (1971) 719–722.
[54] A. Hiraki, Formation of silicon oxide over gold layers on silicon substrates, J. Appl. Phys. 43 (1972) 3643.
[55] H.G. Tompkins, M.R. Pinnel, Relative rates of nickel diffusion and copper diffusion through gold, J. Appl. Phys. 48 (1977) 3144.
[56] U. Gösele, Growth kinetics of planar binary diffusion couples: “thin-film case” versus “bulk cases”, J. Appl. Phys. 53 (1982) 3252.
[57] G. Ottaviani, Review of binary alloy formation by thin film interactions, J. Vac. Sci. Technol. 16 (1979) 1112.

[58] C. Canali, F. Catellani, G. Ottaviani, M. Prudenziati, On the formation of Ni and Pt silicide first phase: the dominant role of reaction kinetics, Appl. Phys. Lett. 33 (1978) 187.
[59] G. Ottaviani, M. Costato, Compound formation in metal—semiconductor interactions, J. Cryst. Growth 45 (1978) 365–375.
[60] C. Canali, G. Majni, G. Ottaviani, G. Celotti, Phase diagrams and metal-rich silicide formation, J. Appl. Phys. 50 (1979) 255.
[61] E.G. Colgan, B.Y. Tsaur, J.W. Mayer, Phase formation in Cr-Si thin-film interactions, Appl. Phys. Lett. 37 (1980) 938.
[62] K.N. Tu, Interdiffusion in thin films, Annu. Rev. Mater. Sci. 15 (1985) 147–176.
[63] K.N. Tu, G. Ottaviani, U. Gösele, H. Föll, Intermetallic compound formation in thin-film and in bulk samples of the Ni-Si binary system, J. Appl. Phys. 54 (1983) 758.
[64] A.D. Smigelkas, E.O. Kirkendall, Zinc diffusion in alpha brass, Trans. Am. Inst. Min. Metall. Eng. 171 (1947) 130–142.
[65] A. Paul, T. Laurila, V. Vuorinen, S.V. Divinski, Thermodynamics, Diffusion and the Kirkendall Effect in Solids, Springer International Publishing, Cham, 2014.
[66] H. Springer, A. Kostka, J.F. dos Santos, D. Raabe, Influence of intermetallic phases and Kirkendall-porosity on the mechanical properties of joints between steel and aluminium alloys, Mater. Sci. Eng. A 528 (2011) 4630–4642.
[67] J. Brillo, H. Kuhlenbeck, H.-J. Freund, Interaction of O2 with WC(0001), Surf. Sci. 409 (1998) 199–206.
[68] L. Chen, D. Yi, B. Wang, H. Liu, C. Wu, Mechanism of the early stages of oxidation of WC-Co cemented carbides, Corros. Sci. 103 (2016) 75–87.
[69] Y. Kumagai, Y. Enatsu, M. Ishizuki, Y. Kubota, J. Tajima, T. Nagashima, H. Murakami, K. Takada, A. Koukitu, Investigation of void formation beneath thin AlN layers by decomposition of sapphire substrates for self-separation of thick AlN layers grown by HVPE, J. Cryst. Growth 312 (2010) 2530–2536.
[70] J.R. Lloyd, S. Nakahara, Formation and growth of voids and/or gas bubbles in thin films, Thin Solid Films 93 (1982) 281–286.
[71] B. Gault, M.P. Moody, J.M. Cairney, S.P. Ringer, Atom Probe Microscopy, Springer, New York, 2012.
[72] T.F. Kelly, M.K. Miller, Invited review article: atom probe tomography, Rev. Sci. Instrum. 78 (2007) 31101.
[73] M.K. Miller, Atom Probe Tomography, Springer, US, Boston, MA, 2000.
[74] M. Thuvander, On the accuracy of compositional quantification for atom probe tomography, Microsc. Microanal. 22 (2016) 642–643.
[75] D. Hudson, G.D.W. Smith, B. Gault, Optimisation of mass ranging for atom probe microanalysis and application to the corrosion processes in Zr alloys, Ultramicroscopy 111 (2011) 480–486.